JOURNAL OF PROPULSION AND POWER
Vol. 26, No. 3, May–June 2010

Direct Numerical Simulations of the Transitional/Turbulent Wake of a Flat Plate

Man Mohan Rai*
NASA Ames Research Center, Moffett Field, California-94035

DOI: 10.2514/1.47244

The near wake of a flat plate with a circular trailing edge is investigated via direct numerical simulations. The boundary layers on both the upper and lower surfaces toward the end of the plate are turbulent. Earlier experimental investigations have used thin plates with turbulent boundary layers to create the wake. This results in large θ/D values (θ is the momentum thickness toward the end of the plate and D is the diameter of the trailing edge). Here the emphasis is on relatively thick plates with blunt trailing edges, which result in θ/D values less than unity. Such flows are of considerable engineering interest, particularly in turbomachinery. The computations are performed with a high-order accurate upwind-biased finite-difference scheme that has been successfully used in the past for direct numerical simulations of cylinder wakes and transitional/turbulent flow on flat plates and turbine airfoils. The simulation is modeled after an experiment. Both the Reynolds number based on the boundary-layer thickness at the end of the plate and Re_D closely approximate experimental data. The ratio θ/D is about 0.05. Computed turbulence statistics both in the plate boundary layer and in the wake are compared with experimental data. Contours of the time-averaged and instantaneous velocity and vorticity fields in the wake are also provided and compared with those obtained for cylinder wakes.

Introduction

THE ability to accurately compute wake flows is of considerable engineering importance. Here we illustrate this point using a recent example involving the space shuttle main engine. The system under consideration is an axial turbine with liquid oxygen as the working fluid: the low-pressure oxidizer turbopump. Inspection of the first row of vanes in this turbine showed evidence of high cycle fatigue (HCF) at the trailing edge near the end-walls. Computational fluid dynamics (CFD) analysis of the known sources of HCF indicated vortex shedding as the most probable cause [1]. It was found that the shedding frequency range overlapped the vane trailing-edge flapping-mode natural frequency. At the present time the first vane of the LPOTP is replaced at carefully monitored time intervals, thus ensuring the safety of the shuttle flights [1]. A first attempt at redesigning the vane is reported in [1]. The objectives pursued were increased vane strength, decreased shedding amplitude, decoupling of the shedding and vane natural frequencies, minimal impact on downstream rows, and performance robustness to manufacturing tolerances. The design assessment reported in [1] indicated that all of these objectives were achieved in substantial measure.

Given the complexity of the underlying physics of the near and intermediate wake, four different codes and turbulence models were used in [1] to compute the flow around the baseline and optimized airfoils in order to assess the reduction in fluctuating amplitude of the trailing-edge surface pressure. All of the codes solve the Reynolds-averaged Navier–Stokes (RANS) equations in conjunction with various turbulence models to provide time-accurate simulations of the flow through the LPOTP turbine. These turbulence models have been validated and used effectively for several classes of flows over a period of years. However, the flow complexities of the very near wake (less than three diameters downstream of the cylinder) and limitations of the turbulence models in computing this region of the wake must be kept in mind in evaluating the results presented in [1]. The LPOTP-assessment computations showed the persistence of a strong laminarlike vortex street more than 40 trailing-edge diameters downstream of the vane trailing edge. Both computations and experiments discussed later in the text indicate that this is not an accurate depiction of the real physics of this flow. A remarkable finding in [1] is that all of the codes and corresponding turbulence models indicate essentially the same qualitative trends in flow quality and significant performance improvements for the redesigned airfoil. However, these RANS simulations were only used to provide a preliminary assessment of the improved wake characteristics. Detailed experiments and numerical simulations that accurately capture the complex physics of wakes are required to fully understand the wakes of the baseline and optimized airfoils. Among the computational approaches that are available for this exercise, direct numerical simulations (DNS) are particularly suitable because they do not require any modeling of turbulence and transition. Fortunately, the Reynolds number in the LPOTP is moderate, and a part-span DNS can be obtained in a reasonable amount of time on current supercomputers.

There is considerable interest in obtaining a basic understanding of the complex underlying physics of transitional/turbulent wakes because of a critical need in aeronautical engineering and other disciplines to predict component/system performance and reliability. Extensive experimental and some computational and theoretical investigations of cylinder wakes have been conducted to better understand such flows. References [2–19] represent some of the pertinent investigations in cylinder wake flow. They include theoretical, experimental, and computational research in near and intermediate wake-velocity statistics, shear-layer instability, Reynolds-number dependence of wake dynamics, and other features of interest. The computational investigations of cylinder wakes included in this list also focus on algorithms and related issues such as accuracy, resolution, and grid topologies. A more detailed review of these articles is provided in [18,19]. The Reynolds number (Re_D, based on cylinder diameter) in all these references except [2] is low (less than 15,000). An extensive analysis of a case where $Re_D = 140,000$ (high subcritical Reynolds number) is provided in [2]. An extensive list of investigations of cylinder flow is provided in [2] and a review of a large body of experimental and computational investigations can be found in [17]. While much has been accomplished there are many important issues that need to be resolved. The very near wake (less than three diameters downstream) comprising the two detached shear layers, the recirculation region, and wake flow is perhaps the most complex; the

Presented as Paper 5215 at the 44th AIAA/ASME/SAE/ASEE Joint Propulsion Conference, Hartford, Connecticut, 21–23 July 2008; received 17 September 2009; revision received 15 December 2009; accepted for publication 15 December 2009.

*Senior Scientist for Computational Sciences, Exploration Technology Directorate. Associate Fellow AIAA.

interaction among these three components is to some extent still a matter of conjecture.

A few large eddy and direct numerical simulations of cylinder wakes have appeared in the literature in the recent past. These investigations focus on the low Reynolds-number range, in which the cylinder boundary layer is laminar (subcritical range). However, from an engineering point of view, there is considerable interest in the situation in which the upper and/or lower boundary layer of an airfoil is turbulent, and these turbulent boundary layers separate from the airfoil to contribute to the formation of the wake downstream. In the case of cylinders with small to moderate diameters, this only occurs at relatively large-unit Reynolds numbers. However, in the case of airfoils, the boundary layer has the opportunity to transition to turbulence on the airfoil surface at a substantially lower-unit Reynolds number because the characteristic length of the airfoil is typically one to two orders of magnitude larger than the trailing-edge diameter. This transition to turbulence would occur unless there is a strong favorable pressure gradient that results in the boundary layer remaining laminar or transitional over the surface of the airfoil.

The majority of the published data for turbulent wakes that are preceded by turbulent boundary layers deals with thin plates. One of the earliest investigations in this area is presented in [20]. Measurements in the turbulent wake of a thin flat plate are provided therein. The boundary layer at the end of the plate is fully turbulent. The ratio of the momentum thickness of the boundary layer to the trailing-edge thickness of the plate (θ/D) is 23.2. The thickness of the trailing edge in wall coordinates (based on the wall-shear velocity at the end of the plate) is 3.0 and is hence smaller than the viscous sublayer. The turbulent boundary layers merge to form the wake. Large-scale Karman vortex formation is not observed in this situation. Experimental data provided in this article include mean velocity and turbulence intensity profiles at several streamwise locations along the wake. A direct numerical simulation of turbulent flow over an infinitely thin flat plate and the associated near wake, which closely approximates the experiment of [20], is described in [21]. The computed profiles of the Reynolds stresses in the cross-stream direction at various locations in the near wake agree well with the experimental data of [20].

Several of the investigations that followed in the wake of the study of [20], such as the experimental investigation of [22] and the analyses of [23,24], are reviewed in detail in [25]. One of the salient findings in these studies is that the wake is characterized by three different regions: the near wake ($x/\theta < 25$), which shows an inner wake sandwiched between the two just-separated boundary layers, in which both wake thickness and velocity grow rapidly and only small-scale mixing is found; an intermediate wake ($25 < x/\theta < 350$), in which the growth rates are smaller and mixing occurs between the outer layers of the original boundary layers; and the self-similar far wake ($x/\theta > 350$), which has been studied extensively. It is also proposed that the centerline velocity in the near wake scales as the wall-friction velocity of the upstream boundary layer and the streamwise distance expressed in wall units. While the centerline velocity in this region is proposed to vary as $x^{1/3}$, in the intermediate region it increases logarithmically like the velocity in the turbulent boundary layer. The velocity profiles in the cross-stream direction are found to be close to that of the turbulent boundary layer in the near wake, but begin to lose their logarithmic behavior as one moves downstream and the inner wake continues to grow. The intermediate wake shows a continuing increase of the maximum shear stress in the profile with increasing distance, but possesses the property of local similarity in that profiles of Reynolds shear stress normalized by the local maximum closely approximate the far-wake distribution.

Flow visualization and velocity measurements of the near and intermediate wakes for a thick plate with a tapered trailing edge (taper half-angle of 4°) with fully turbulent boundary layers are provided in [26]. It is found that the low-speed streaks of the near-wall turbulent boundary layer persist in the near wake for about 130 wall units in the streamwise direction. Further downstream these structures seem to lose their directionality, and their spanwise scale was found to increase; in particular, the turbulent flow structures at the location $x^+ = 1070$, $y^+ = 270$ in the wake (away from the centerline) were found to closely resemble those found in the upstream boundary layer at $y^+ = 130$. One of the important findings of this study is that the analogy between the velocity profile obtained for the zero-pressure-gradient turbulent boundary and the wake-centerline velocity is much stronger than suggested by any of the earlier investigations. It is found that a transformation of the type $y^+ = Kx^+$ (K lies between 0.1 & 0.12 for the case studied) essentially collapses both the linear and logarithmic portions of the turbulent boundary-layer velocity profile onto the wake profile. Experimental data obtained in this investigation in the very near wake ($x^+ < 100$) permits the verification of the linear variation of wake velocity with x in this region. This refutes the $x^{1/3}$ variation proposed in [24] (interestingly, the DNS of [21] yields an exponent of $1/2$ for the infinitely thin plate). The authors also note the presence of a very small region near the trailing edge ($x^+ < 15$), in which unsteady vortex shedding was noticed intermittently. These shed vortices were dominated by larger streamwise vortices associated with the turbulent flow. One feature that this experiment shares with the earlier experiments is a rather large ratio of θ/D in spite of the thick plate.

In many instances, unlike the experiments discussed above, the ratio of the momentum thickness of the boundary layer at the trailing edge to the trailing-edge dimension is not large. For reasons of manufacturability, cost, and reliability, the ratio is much smaller; that is, the trailing-edge thickness is larger than the boundary-layer momentum thickness. Ratios close to or smaller than one are of interest from an engineering point of view. The emphasis in this study is the investigation of transitional/turbulent wakes in situations where θ/D is smaller than unity. Here, the boundary layers do not merge smoothly to form the wake as in the large θ/D case but form detached shear layers that are susceptible to instabilities, which in turn results in the breakdown of the shear layers. Large-scale Karman vortex formation is also present. Smaller-scale turbulent structures are found embedded in the larger Karman vortices. Thus, these wake flows share some attributes with low to moderate Reynolds-number cylinder wake flows ($1200 \leq Re_D \leq 150,000$) that have been studied extensively. However, one major difference between the two is that the boundary layer in the small θ/D cases studied here is turbulent even though the Reynolds number based on the trailing-edge diameter is relatively small.

Unlike the large θ/D case, there seems to be a scarcity of experimental investigations for small θ/D ($\theta/D < 1$). One noteworthy example of this latter case is provided in [27]. This experimental investigation was conducted simultaneously with [26] by the same authors and thus inherits most of the general test conditions from [26], the main difference being the use of a circular trailing edge instead of a tapered wedgelike trailing edge. The value of θ/D is about 0.05. This results in large-scale Karman vortex shedding and thus near-wake flow that does not resemble the experimental investigations discussed earlier. However, it is representative of the wake flows commonly found in turbomachinery and other flows of engineering interest, and it thus constitutes a valuable resource, both in understanding the physics and providing a basis of comparison for subsequent experimental and computational investigations. The findings of [27] will be discussed in detail in a later section.

Here, we use a high-order accurate, upwind-biased finite-difference method for curvilinear grids to compute the flow over a thick flat plate with a circular trailing edge. The laminar boundary layer on the flat plate undergoes transition and becomes turbulent downstream. The flow is turbulent when it encounters the trailing edge. The computation is modeled after the experiment of [27]. Both the Reynolds number based on the boundary-layer thickness at the end of the plate and Re_D closely approximate those of [27] ($Re_\delta \approx 16,000$, $Re_D \approx 32,000$). The ratio θ/D is 0.05. The main features of both the investigations are expected to be similar, although some differences can be expected in quantitative comparisons between mean velocity and turbulence intensity profiles in the wake. The goals here are to initiate the computational study (via DNS) of turbulent wakes preceded by turbulent boundary layers in the context of thick, blunt trailing edges (small θ/D), investigate near-wake flow physics, and compare the computed results with experimental data.

Computational Grid

The computational region is divided into two zones to facilitate grid generation and provide adequate grid resolution for the wake. Figure 1 shows the plate cross section and the two zones that together comprise the computational region. The three-dimensional zones and grids are obtained by uniformly spacing copies of their two-dimensional counterparts in the spanwise direction z. The plate zone is bounded by four boundaries: the plate surface (excluding the trailing edge), an external boundary, and two zonal boundaries (left and right) which interface with the wake zone. It captures the inviscid flowfield upstream of the trailing edge and the boundary layer on the plate. The leading edge of the plate is an ellipse. The wake zone is constructed to provide optimum grid resolution for the detached shear layers, the recirculation region, and the wake of the plate. The boundaries of this zone include the circular trailing edge, the left and right boundaries, and the exit boundary. Both the left and right boundaries consist of a zonal boundary segment that interfaces with the plate zone and a second segment that serves as an external boundary.

Three different grids were used to perform the simulations reported in this investigation. These grids were generated with an algebraic grid generator. Figure 2 shows representative grids in the vicinity of the trailing edge in both zones. The grid in the wake zone transitions from curvilinear near the trailing edge to rectangular downstream. The external boundary of the plate zone is placed $10.0D$ from the plate surface, where D is the diameter of the circular trailing edge (D is also the thickness of the plate). The length of the plate is $25.5D$. The exit boundary of the wake zone is placed $102.75D$ from the center of the circular trailing edge, and the cross-stream extent of this boundary is $58.5D$. In the vicinity of the trailing edge, where the left and right boundaries of the wake zone are parallel to the x axis, the cross-stream extent of this zone is $6.5D$ and is large enough to completely contain the computed wake. The spanwise dimension of the computational region is $\pi D/2$. The streamwise extent of the well-resolved region of the wake extends to $10.0D$ (from the center of the circular trailing edge), although the region of interest in this computation is only up to $6.5D$. The fine grid continues further than required to minimize any effect of grid coarsening, which begins at $10.0D$, on the computed wake in the first 6.5 diameters. Beyond $10.0D$, the grid coarsens gradually in both the streamwise and the cross-stream directions. In addition to reducing the computational costs incurred, this coarsening dissipates the wake to a degree that inviscid boundary conditions can be used at the exit boundary of the wake zone.

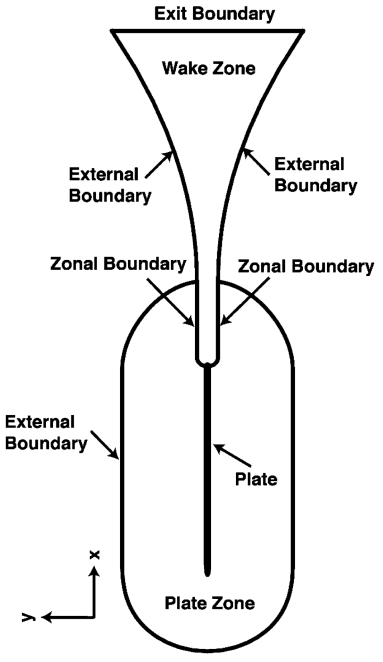

Fig. 1 Midspan plate section and multiple zone discretization of the computational region.

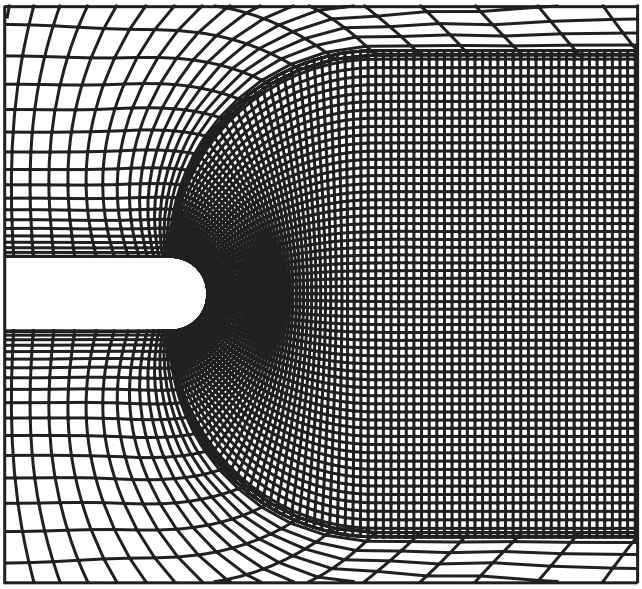

Fig. 2 Representative grids in the plate and wake zones, in the vicinity of the trailing edge.

The baseline wake grid was constructed with 451 grid points in the streamwise direction, 221 in the cross-stream direction, and 256 in the spanwise direction ($451 \times 221 \times 256$). At $x/D = 6.5$, the resolutions achieved along the centerline in these directions are approximately $\Delta x/\eta = 6.0$, $\Delta y/\eta = 6.0$, and $\Delta z/\eta = 1.2$, respectively. Here, η is the estimated Kolmogorov length scale at $x/D = 6.5$. The spacing in the y direction Δy increases slightly from the centerline to the left and right boundaries of the wake grid. The baseline plate grid was constructed with 1501 points in the wall tangential direction, 81 points in the wall normal direction, and 256 points in the spanwise direction. The grid spacing in the x and z directions are approximately 28.0 and 8.6 wall units, respectively, based on the wall-shear velocity near the end of the plate. The grid spacing in the y direction at the plate surface is 1.04 wall units. The total number of grid points used to generate the baseline grid was 56,640,512. The results obtained on this grid are labeled *BG* (baseline grid) in the following sections.

The computation on the fine grid was performed as a grid-refinement exercise. The wake grid in this case was constructed with 601 points in the streamwise direction, 331 points in the cross-stream direction, and 256 points in the spanwise direction. At $x/D = 6.5$, the resolutions achieved along the centerline in these directions are approximately $\Delta x/\eta = 4.0$, $\Delta y/\eta = 4.0$, and $\Delta z/\eta = 1.2$, respectively. As before, the well-resolved wake grid extends 10 diameters from the center of the trailing-edge circle. The refined plate grid was constructed with 2501 points in the wall tangential direction, 81 points in the wall normal direction, and 256 points in the spanwise direction. The grid spacing in the x and z directions are approximately 19.2 and 10.0 wall units, respectively, based on the wall-shear velocity near the end of the plate. The grid spacing in the y direction at the plate surface is 0.92 wall units. The results obtained on this grid are labeled *FG* (fine grid) in the following sections. The total number of points used in grid FG is approximately 103 million.

Adequate mesh resolution in the streamwise direction in grids BG and FG exists only on the second half of the plate. Flow transition (end-stage transition) is achieved by about 55% chord on these grids (shape factor is about 1.4 at this streamwise location). In the experiment [27], flow trips were positioned at 30% chord. Information regarding the region of transition is not provided in [27]. To determine the effect of an early transition (around 30% chord) the DNS was performed on a third grid labeled EBG (extended baseline grid). The grid used in the wake zone in EBG is the same as that in BG. However, in EBG, the entire length of the plate is provided with a grid that is fairly well-resolved in the streamwise direction. The plate

grid is constructed with 2501 points in the streamwise direction, 81 in the cross-stream direction, and 256 in the spanwise direction. The grid spacing achieved in these directions (at the wall in the cross-stream direction) are 32.2, 0.98, and 9.6 wall units, respectively. Flow transition on this grid was achieved at about 30% chord. The total number of grid points in EBG is 77,376,512.

At the zonal boundaries, the two zones interface along common grid lines, thus reducing the information transfer procedure from a two- to a one-dimensional interpolation. For example, the left zonal boundary of the wake grid coincides with an inner grid line in the plate grid. However, the grid points along this common grid line do not coincide. A similar situation exists at the other zonal boundaries.

Numerical Method and Boundary Conditions

In [28], the high-order accurate upwind-biased method of [29], which was used to compute transitional flow on a flat plate using rectangular grids, is extended to curvilinear grids. In [18], a version of the method of [28] is used to perform a direct numerical simulation of cylinder wake flow ($Re_D = 3900$). The principal goal of this effort was to investigate the claim that high-order upwind methods may be too dissipative on the generally coarser grids that are used both for (large-eddy simulations) LES and coarse-grid DNS simulations. Computed turbulence intensity profiles in the cross-stream direction and centerline velocity spectra were found to agree well with the experimental data of [7]. The computed results were not negatively impacted by the dissipation of the upwind-biased scheme on the grid used for the simulation. The number of grid points used in this computation was nearly the same as that used in the medium-resolution B-spline computations of [12], which yielded wake-velocity spectra and statistics that compared well with the experimental data of [7] in the first 10 diameters downstream of the cylinder. It can also be inferred from [18] that using roughly the same number of grid points as in [8], in which numerical dissipation resulted in reduced solution accuracy, will still result in the same superior wake-solution accuracy with the finite-difference method of [18]. A second computation is provided in [18] that computes the wake flow up to $x/D \leq 40.0$ ($Re_D = 5830$). The computed intensity profiles are compared with the experimental data of [5] and are found to be in agreement even at $x/D = 40.0$.

In [18], the cylinder computations at $Re_D = 3900$ were performed on both a baseline grid and a fine grid. The fine grid contained approximately twice as many grid points as the baseline grid. Turbulence statistics and velocity spectra obtained in the wake on these two grids were compared in [18]. Only minor differences are noted between the two sets of results, thus essentially establishing grid independence of the computed data. The results obtained in [18] demonstrate that upwind-biased methods with the requisite order of accuracy, operating on grids with the necessary grid density, are capable of yielding accurate solutions not only in the context of DNS but also on relatively coarser grids, which would be considered adequate for LES.

The high-order accurate upwind-biased method developed in [18] is used here to compute the flow over the plate as well as in the wake. As mentioned earlier the computational region is discretized using two grids: the plate grid and the wake grid. The boundaries that contain these grids can be broadly classified as natural and zonal boundaries. The natural boundaries include the external boundary of the plate grid, the surface of the plate, the exit boundary of the wake grid, the segments of the left and right boundaries of the wake grid labeled as *external boundary* in Fig. 1, and the boundaries in the spanwise direction. The upstream segment of the left boundary between the plate and wake grids is an example of the zonal boundaries used in the computation. Both the natural- and zonal-boundary conditions used in this study are discussed in [18,28]. No-slip/adiabatic wall conditions are used on the plate surface and the trailing-edge circle. Wall blowing/suction, as described in [28], is implemented on a short segment on both the surfaces of the plate between the leading edge and midchord to induce transition to turbulence.

Results

The plate computations were performed at a Mach number of 0.1. The unit Reynolds number is 8000 per inch. The plate length, trailing-edge-circle diameter, and unit Reynolds number are nearly the same as in the experiment [27]. Initial transients were eliminated by integrating the governing equations over a period of time corresponding to several trailing-edge vortex-shedding periods. Turbulence statistics were averaged both in time and in the spanwise direction over a period of eight shedding cycles. The computed and experimental Strouhal numbers are 0.22 and 0.21, respectively.

As discussed in the introduction there is a large body of literature that deals with cylinder wakes. Additionally, there are at least a few investigations of the wakes of thin flat plates (large θ/D). We begin this section by providing some motivation for investigations of thick flat plates with blunt trailing edges (turbulent boundary layers, small θ/D). Figure 3 shows contours of time-averaged spanwise vorticity in the wake of a cylinder at $Re_D = 3900$ obtained from a DNS. Several experimental and computational studies of cylinder wakes have been performed at this Reynolds number. The detached shear layers are clearly visible in this figure. Figure 4 shows corresponding contours from a flat-plate (circular-trailing-edge) DNS, in which the Reynolds number is 3900 based on the thickness of the plate and the boundary layers on both the upper and lower surfaces are turbulent. Details regarding these computations are provided in [30]; here, we discuss the results obtained from these computations briefly. The minimum and maximum values of spanwise vorticity and the vorticity increment between successive contours in Figs. 3 and 4 are the same. Clearly, the detached shear layers in the latter case are much shorter; they undergo transition and breakdown earlier because of the large disturbances contained within the detaching boundary layer. This is similar to cylinder cases at much higher Reynolds numbers.

Another feature of interest is that the cylinder-detached shear layers have a bowed shape, whereas in the case of the plate they are straighter and are oriented toward the centerline. The laminar cylinder boundary layers detach before the vertical at the center and therefore exhibit a positive slope. In the case of the plate, the turbulent boundary layer detachment occurs at about 22.2 degrees past the vertical. One consequence of this difference in shape is that fluid on the free-streamside of the cylinder shear layers accelerates (streamwise velocity about 30% higher than free-stream velocity). In the case of the plate this increase in streamwise velocity is minimal (less than 3%) and is only observed very near the base of the cylinder. In addition to these differences the computed values of the mean square fluctuating velocity components along the wake centerline for the cylinder, in the first ten diameters downstream of the trailing edge, at $Re_D = 3900$, are consistently two to four times larger than the corresponding values for the flat plate.

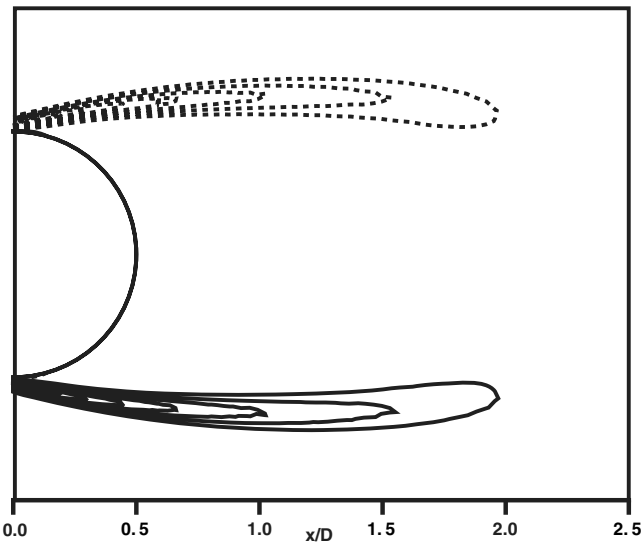

Fig. 3 Contours of time-averaged spanwise vorticity for the cylinder, $Re_D = 3900$.

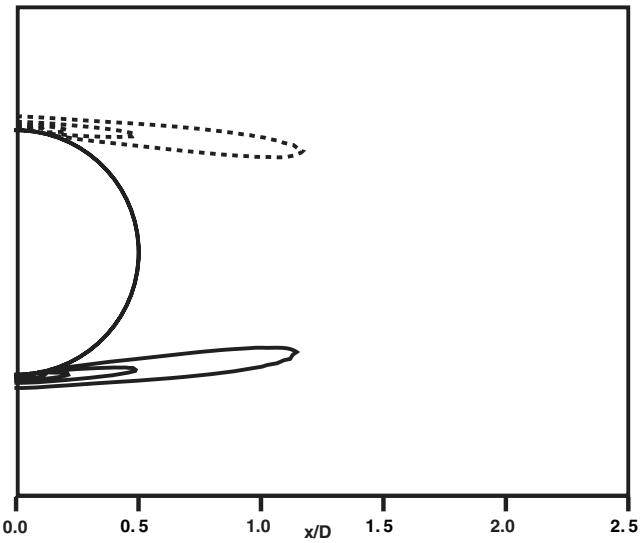

Fig. 4 Contours of time-averaged spanwise vorticity for the flat plate, $Re_D = 3900$.

In both the cylinder and flat-plate cases discussed above the cross-stream Reynolds-stress component is much larger than the streamwise component along the wake centerline. However, this is not the case for the thin plate. The thin plate results show the cross-stream component to be smaller than the streamwise component. The main reason for this difference is the presence of vortex shedding in the small θ/D cases. In addition, velocity profiles at various streamwise locations for the thin plate do not show any recirculation region. Instead, they show a smooth monotonic progression from two turbulent boundary-layer profiles at the trailing edge to a wake profile downstream. Further, both the Reynolds-stress components obtained for the plate and the cylinder along the wake centerline are similar in that they increase rapidly from the base of the cylinder, reach a peak between $1.4D$ and $2.5D$ and subsequently decrease rapidly until about $x/D = 7.0$, and then continue to decrease much more gradually. This is in contrast to the case of the thin plate, in which the components continuously decrease with increasing distance from the trailing edge (except for a small region near the trailing edge). Very near the trailing edge ($x^+ < 300$), the data of [26] shows the streamwise component first increasing and then decreasing with increasing distance along the centerline, with the peak occurring in the region $100 < x^+ < 200$.

The main objective of the comparisons made here with the thin-plate results and those of the cylinder is to establish the fact that the thick plate while possessing aspects of both the aforementioned flows has its own unique features and deserves investigation. It is particularly important because so many practical applications such as turbomachinery airfoils share some important features with the thick flat plate with a blunt trailing edge. Mean velocity and turbulence intensity profiles at various streamwise locations in the near and intermediate wake, for the cylinder and thin plates at different flow conditions, are available in the literature. They aid in our understanding of wake flows, in turbulence model development and algorithm/code validation efforts. One of the goals of the current investigation is to establish a DNS database for thick plates with circular/blunt trailing edges ($\theta/D < 1.0$).

The Case $ReD = 32,200$

Results for the Plate Section

Although the principal objective here is the investigation of the transitional/turbulent wake of the flat plate, it is necessary to establish that the plate boundary layer is indeed turbulent before it detaches from the plate surface and merges with the wake flow. Figure 5 shows instantaneous spanwise velocity contours on the upper surface of the plate (grid FG). The transition from laminar to turbulent flow at about 50% chord ($x/c = -0.5$) is evident. End-stage transition is

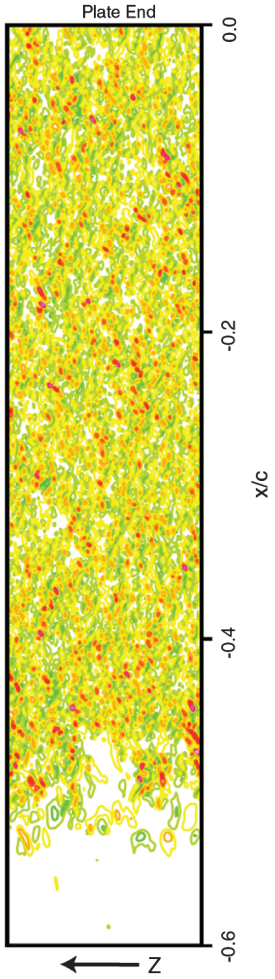

Fig. 5 Instantaneous contours of spanwise velocity w above the plate surface, FG.

characterized by a relatively sharp boundary (which fluctuates in time). The flow on the lower surface of the plate is very similar. The features seen here are similar to those reported in [29], in which flat-plate flow transition induced by high levels of free-stream turbulence is computed from first principles via DNS.

Figure 6 shows the variation of the shape factor along the length of the plate obtained on grids BG and FG. End-stage transition is essentially complete at about 60% chord ($x/c = -0.40$). The computed value of the shape factor on both the grids is about 1.4 at this location. Further downstream, the shape factor continues to decrease very gradually to about 1.33 at 96% chord (the experimental value at this location, $x/c = -0.04$, is 1.43). A more rapid decrease is obtained in the last 4% of chord. This is consistent with a favorable pressure gradient in this region, which is discussed in the following

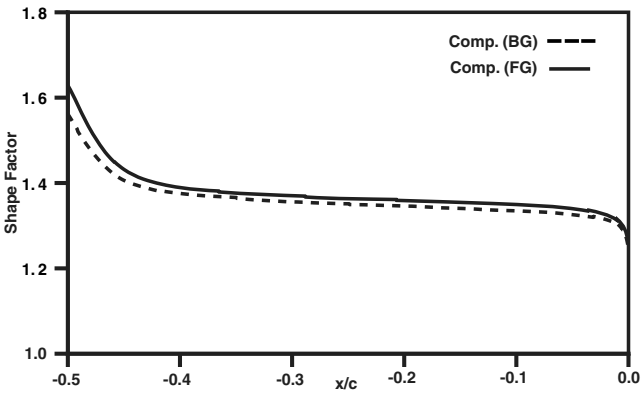

Fig. 6 Shape factor distribution along the length of the plate.

figures. The results of Fig. 6 clearly indicate that the flow at the trailing edge is turbulent and that additional increases in grid resolution, above that of grid FG, will have little effect on the computed distribution of the shape factor.

The momentum thickness (θ/D) toward the end of the plate reported in [27] is 0.05. The computed values of θ/D on both BG and FG were about 0.04 and thus slightly lower than the experimental data. The main objective of the computation on the grid EBG was to ascertain if earlier flow transition would yield the experimentally obtained momentum thickness. As mentioned earlier flow trips were positioned at about 30% chord in the experiment. Assuming that transition occurred soon thereafter, the computed transition location on EBG (30% chord) and the experimental transition location are in agreement. The value of θ/D obtained on EBG was indeed 0.05 and thus close to the experimental value. Based on this computation it would seem that a grid-refinement exercise on grids that provide adequate resolution in the streamwise direction on the entire length of the plate, so that early transition can be captured, is appropriate. However, grid FG already uses more than 100 million grid points. In the interest of reducing computing costs in this exploratory effort, we have resorted to computations on BG and FG with transition occurring about midchord. The effect of this slightly delayed transition on the plate on wake-velocity statistics is small.

Figure 7 shows computed mean velocity profiles (FG) in the transitional and turbulent regions at various streamwise locations. The dashed lines represent the near-wall linear behavior ($u^+ = y^+$) and the log law ($u^+ = 5.0 + 2.44\,\ell_n(y^+)$), where u^+ is the streamwise component of velocity normalized by the wall-shear velocity and y^+ is the distance normal to the plate surface in wall coordinates. The first profile at $x/c = -0.600$ (the center of the trailing-edge circle is at $x, y = 0.0$) occurs before a rapid increase in skin friction. The next two profiles ($x/c = -0.500$ and -0.475) are from the transitional region, and the last one ($x/c = -0.040$) is in the turbulent region. The profiles change monotonically from laminar-like to turbulent with increasing streamwise distance. The agreement with the linear profile and the log law at $x/c = -0.04$ is good although the computed profile shows a slight overshoot compared with the log law in the region $10.0 < y^+ < 80.0$ (the plate grid requires about 1.5 times the current resolution in the streamwise and spanwise directions in order to yield essentially grid-independent velocity statistics on the plate). The velocity profile at $x/c = -0.04$ does not show much of an outer wake. Fig. 8 shows the time-averaged surface-pressure distribution on the plate section. The pressure decreases rapidly in the vicinity of the leading edge followed by a recompression region that ends downstream of the location at which the leading-edge ellipse merges with the flat plate. The pressure is nearly constant on the plate surface, thereafter followed by a favorable pressure gradient near the trailing edge. The lack of a distinct wake in the boundary-layer profile at $x/c = -0.04$ is consistent with this favorable pressure gradient near the trailing edge.

Figure 9 shows a comparison of the computed velocity profiles obtained on the baseline and fine grids with the experimental data at the streamwise location $x/D = -1.0$ ($x/c = -0.04$). Here, the velocity is normalized with the boundary-layer edge velocity and the distance normal to the wall by the boundary-layer thickness. The computed results are in good agreement with each other but are higher than the experimental data. The reason for this difference is not clear at the present time. It should be noted that the overshoot compared with the log law mentioned earlier exists only for $y/\delta < 0.1$ and at its worst is only half the magnitude of the difference between experiment and computation. Hence, it does not explain this difference. Overall, the agreement between experimental and computational results is fair.

Figure 10 compares the computed streamwise Reynolds-stress profile (BG and FG) with that obtained experimentally at the same streamwise location as in the previous figure. Here again, the profiles obtained on the baseline and fine grids are close. The computed peak values are slightly higher than the experimental one. Everywhere

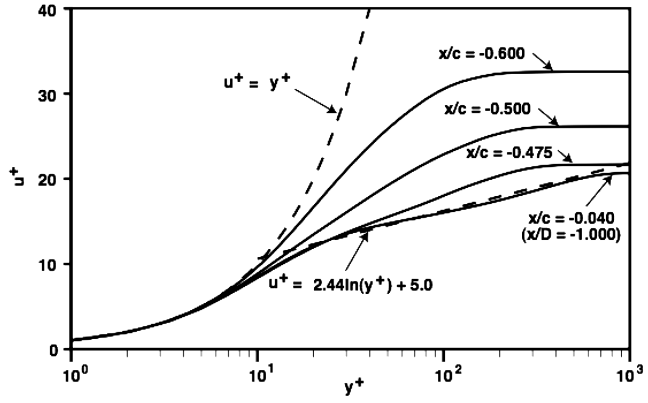

Fig. 7 Mean velocity profiles normalized by wall-shear velocity at various locations on the plate, FG.

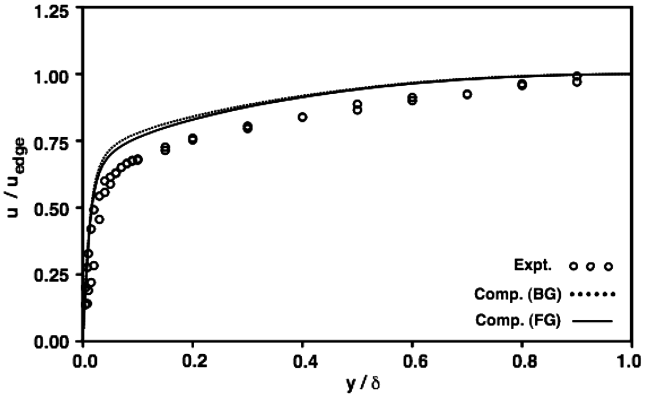

Fig. 9 Mean velocity profile at $x/D = -1.0$, normalized by boundary-layer edge velocity.

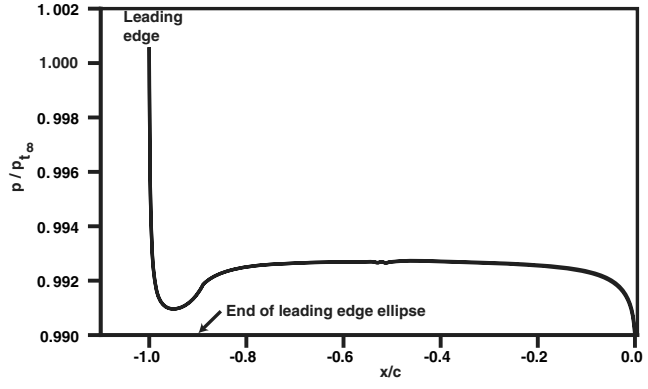

Fig. 8 Time-averaged surface pressure distribution on the plate, FG.

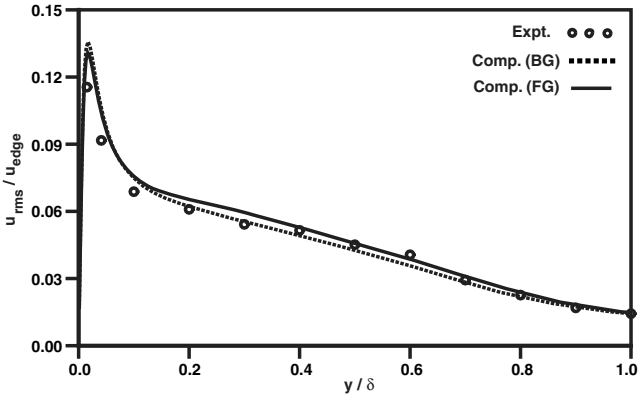

Fig. 10 Streamwise Reynolds stress profile at $x/D = -1.0$, normalized by boundary-layer edge velocity.

else, the agreement between the computed and experimental profiles is good. Figures 6–10 demonstrate that the computed turbulent boundary layer separating from the plate approximates the experimental one fairly closely.

Flowfield Visualization of the Wake

A few snapshots of both the time-varying and time-averaged flowfield are provided here (obtained on grid FG). Figure 11 shows instantaneous contours of the streamwise velocity in an (x, y) plane at one spanwise location. This figure includes the entire region of interest, $0.0 < x/D < 9.0$. Adequate grid resolution extends up to $x/D = 10.0$. The upper and lower detached shear layers are visible. The breakdown of the shear layers and the subsequent transition to turbulence can also be observed. The size of the separated region and the individual lengths of the shear layers fluctuate in time. The mean length of the recirculation bubble is about $0.56D$.

Figure 12 shows instantaneous contours of the cross-stream velocity v in an (x, y) plane for the plate. The Karman vortex street creates regions of alternating positive and negative cross-stream velocity (red/yellow and blue/green). These clearly delineated regions occur because the fluctuating component of the cross-stream velocity is large compared with the mean value and because a significant portion of this fluctuating velocity is coherent. A similar snapshot of v in an (x, z) plane (not shown here) shows bandlike regions of positive and negative v which extend over the entire span.

Figure 13 shows instantaneous contours of the spanwise component of velocity in an (x, y) plane. The effect of Karman shedding is very pronounced here; the wake spreads rapidly in the cross-stream direction. The base region of the cylinder shows considerable small-scale activity compared with lower-Reynolds-number cylinder cases. This small-scale activity is discernible nearly everywhere in the region of interest. The very distinct Karman shedding process, the embedding of the turbulent structures in the Karman vortices, and the clear demarcation between the wake fluid and the outer flow are also evident.

Figure 14 shows instantaneous spanwise vorticity contours near the trailing edge. The detached shear layers are very thin and do not extend beyond the base of the trailing edge. At the instant in time that was chosen, the lower detached shear layer is more extended than the upper one. Its thickness was determined to be about 25 wall units (this comprises only the region corresponding to the high gradient in vorticity and is based on the plate wall-shear velocity close to the trailing edge), thus indicating that it is largely composed of the viscous sublayer of the upstream turbulent boundary layer. The breakdown of the two shear layers can also be seen in Fig. 14.

Contours of the time-averaged spanwise vorticity are shown in Fig. 15. The contours levels coincide with those of Figs. 3 and 4. In comparison, the shear layers obtained in the present case are even shorter, which is consistent with the higher Reynolds number and turbulent boundary layers. As in Fig. 4 the shear layers are oriented

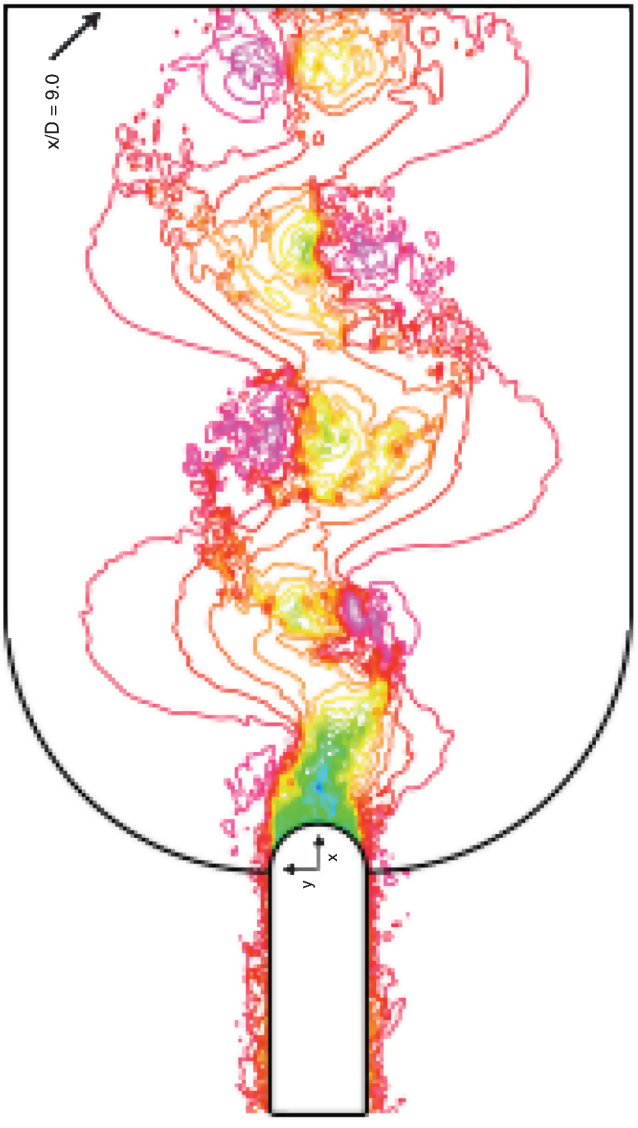

Fig. 11 Instantaneous contours of the streamwise velocity u in an (x, y) plane, FG.

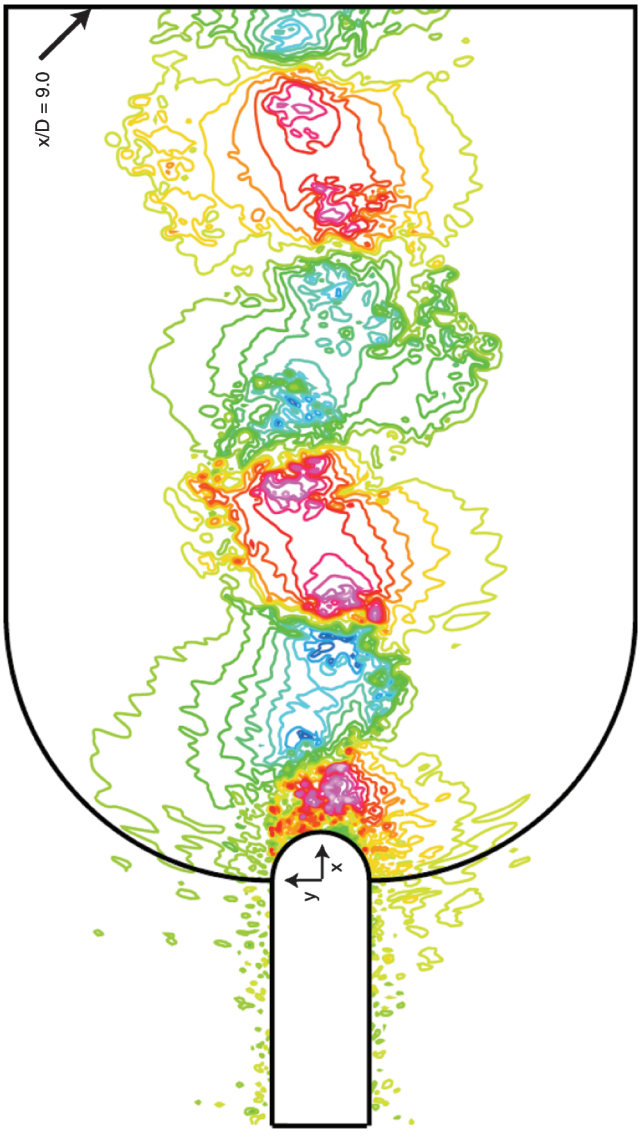

Fig. 12 Instantaneous contours of the cross-stream velocity v in an (x, y) plane, FG.

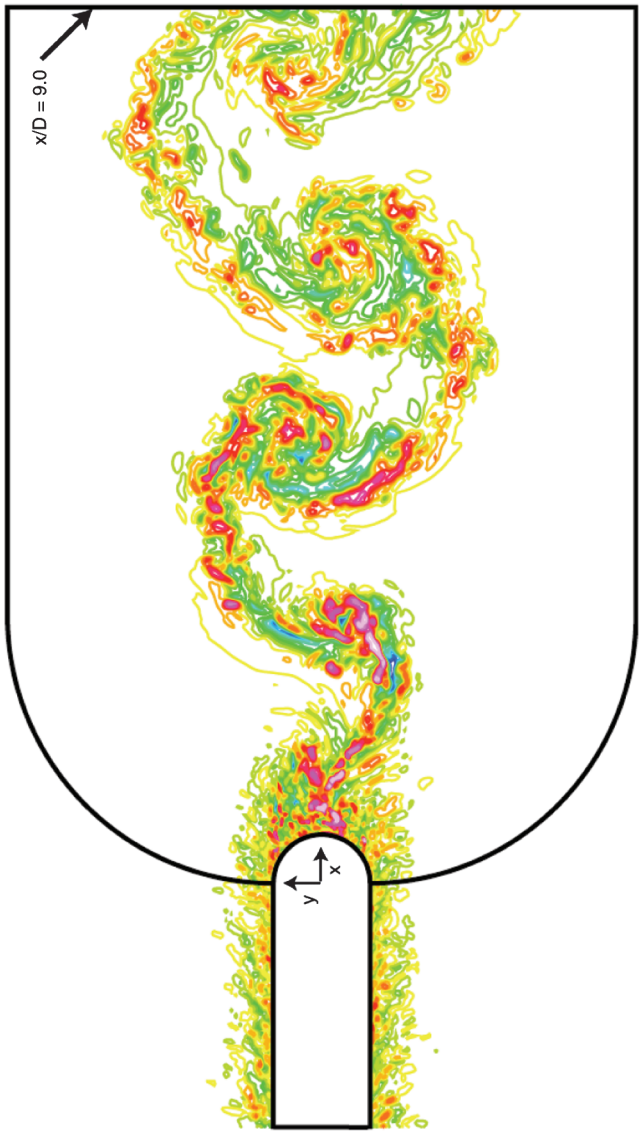

Fig. 13 Instantaneous contours of the spanwise velocity w in an (x, y) plane, FG.

Fig. 14 Instantaneous contours of the spanwise vorticity in an (x, y) plane, FG.

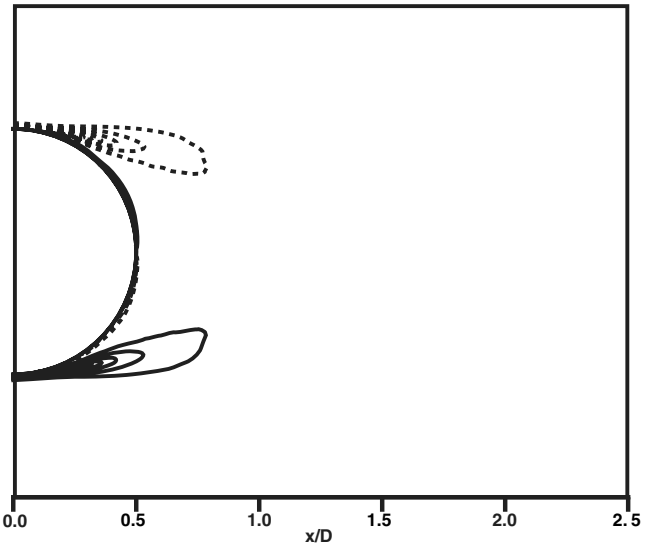

Fig. 15 Time-averaged spanwise vorticity contours for the flat plate, FG.

toward the wake centerline because boundary-layer separation occurs past the vertical line at the center of the trailing-edge circle. Also evident in Fig. 15 is the presence of near-wall vorticity. This was noticeably absent in Figs. 3 and 4. The cylinder computation of [15] at $Re_D = 10,000$ does show near-wall activity.

Figure 16 shows contours of time-averaged streamwise velocity normalized by the free-stream velocity. Here and in Fig. 18, solid lines represent positive contour values, and dashed lines represent contour values less than or equal to zero. The contour lines corresponding to 0.0 and 1.0 have been identified in this figure. The first of these shows the extent of the region of separation as well as the location at which the boundary layer separates from the plate. Clearly, this region is confined to the vicinity of the base. The recirculation region is 0.56 diameters in extent along the wake centerline. Its upper and lower ends are located 15.2 degrees to the right of the vertical. The contour level 1.0 shows that acceleration on the free-stream side of the shear layers is small and confined to the trailing edge region.

Figure 17 shows contours of the streamwise Reynolds stress (u_{rms}/u_∞, containing both coherent and random components of fluctuation) as for the cylinder in [15]. The upper and lower detached shear layers are regions characterized by both high and rapidly varying intensity levels. Another feature of interest is that

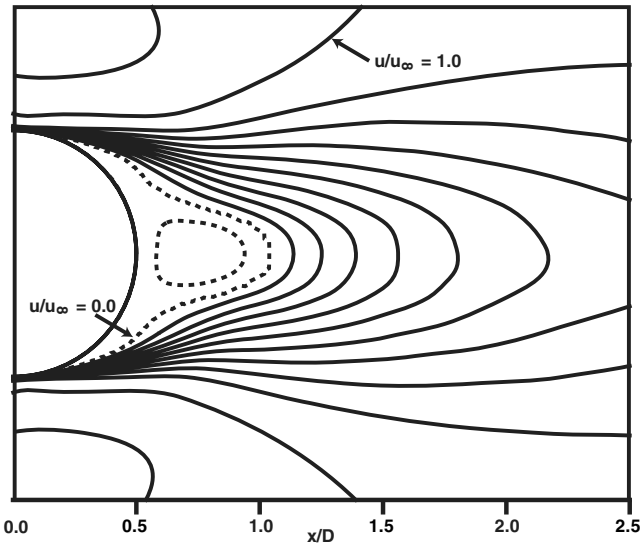

Fig. 16 Time-averaged streamwise velocity contours for the flat plate, FG.

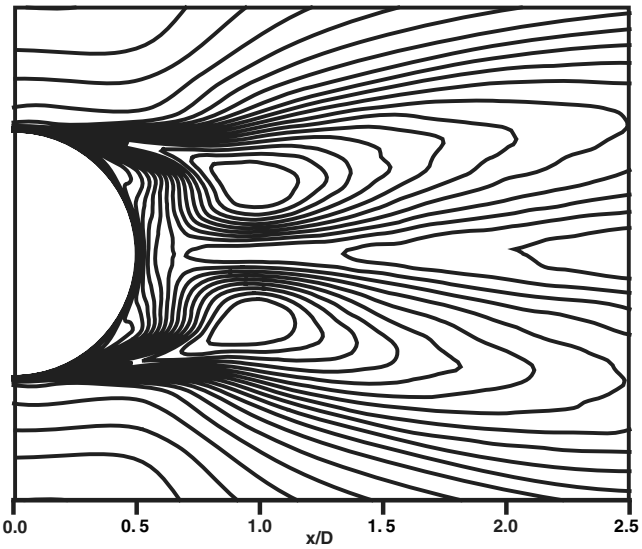

Fig. 17 Time-averaged streamwise Reynolds stress contours for the flat plate, FG.

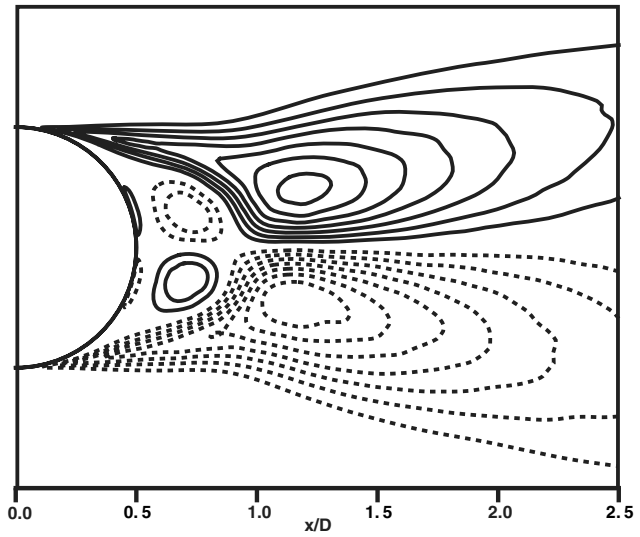

Fig. 18 Time-averaged Reynolds shear stress contours for the flat plate ($-u'v'$), FG.

the maxima occur away from the centerline. Reference [15] provides both experimental and numerical data for the cylinder at $Re_D = 10,000$. These investigations of [15] are at a subcritical Reynolds number, and the detaching boundary layers are laminar. The experimental and numerical peak values are both 0.5. The present computation yields a value of about 0.38. The experimental and numerical values of the streamwise location of the maxima from [15] are $x/D = 1.14$ and 1.13, respectively. The location obtained here is about 0.99.

Figure 18 shows contours of Reynolds shear stress obtained here. Shear stress values are antisymmetric about the centerline. The shape of the contour lines is similar to that obtained in [15]. As pointed out there, these contours show four distinct lobes. The surface maximum and minimum, seen in Fig. 18, are not observed in [15]. The experimental and numerical maximum shear-stress values at $Re_D = 10,000$ are 0.14 and 0.15, respectively, and they occur at $x/D = 1.4$. The current simulation with $Re_D = 32,000$ yields a value of 0.078, approximately half as much, at $x/D = 1.18$. As observed in [15], the elongated regions are indicative of early transition in the shear layer. Here these regions originate in the upstream boundary layer itself because the boundary layer is turbulent; in [15], the tip of the region approximately coincides with the base of the cylinder ($x/D = 0.5$).

Wake Velocity Statistics

Figure 19 compares the computed mean streamwise centerline velocity in the wake with experimental data. The two computed profiles are in close agreement with each other. The length of the region of separation is $0.56D$. The computed data agree fairly well with the experimental data.

Figure 20 shows the computed wake centerline variation of the streamwise and cross-stream Reynolds stresses. Experimental data was only available for the streamwise component. While the two computed profiles of streamwise intensity are in close agreement, the cross-stream intensity profile obtained on the fine grid is slightly higher than that obtained on the baseline grid almost everywhere along the wake centerline. The computed streamwise profiles agree well with the experimental data in the very near wake ($x/D < 3.0$) but are higher further downstream.

Overall, the agreement between the computation and experiment in Figs. 19 and 20 is fair. Since the computed streamwise velocity statistics obtained on the baseline and fine grids agree well, the remaining differences between experiment and computation are probably in part because of differences in setup. The sidewalls of the water channel are located 4.0 diameters from the plate surfaces and 4.5 diameters from the wake centerline. Here, the external boundary is placed $10.0D$ from the plate surfaces, and at $x/D = 6.5$ in the wake zone (where the last comparison is made) it is $8.25D$ from the wake centerline. Second, the depth of the water channel is 3D with water height of $2.5D$ (bounded surface on the lower side and free surface on the upper side). Here, we have used a spanwise length of $\pi D/2$ based on the work of [12] with a periodic boundary condition. While this length is considered to be adequate an additional computation with twice the spanwise dimension would be informative. However, this would require a grid that is twice as large and a correspondingly larger amount of computational resources. We defer this computation to a later study. These observations are relevant to the next six figures, which deal with wake-velocity statistics.

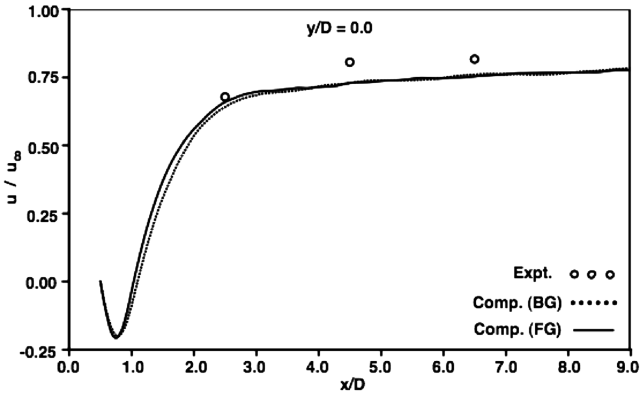

Fig. 19 Variation of the mean streamwise velocity along the wake centerline.

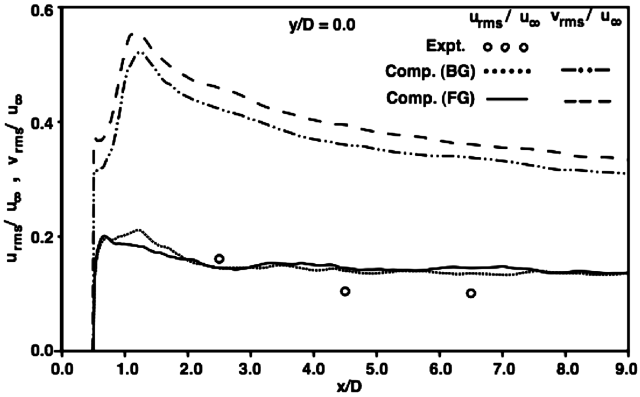

Fig. 20 Variation of the streamwise and cross-stream Reynolds stresses along the wake centerline.

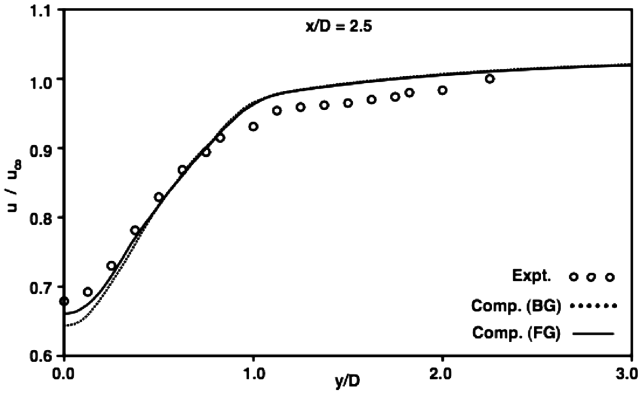

Fig. 21 Profile of mean streamwise velocity at $x/D = 2.5$.

Figures 21–23 show the computed mean streamwise velocity profiles at the locations $x/D = 2.5$, 4.5, and 6.5 in the wake, and the corresponding experimental data [27]. In all these figures the data obtained on the baseline and fine grids show minor differences. The agreement between computation and experiment at the station $x/D = 2.5$ is good. Further downstream, at $x/D = 4.5$ and 6.5, the computed centerline value is lower than the experimental value. The computed profiles at these two latter locations are narrower than their experimental counterparts. Overall, the agreement between computation and experiment is fair.

Figures 24–26 show the computed streamwise and cross-stream Reynolds stresses at the same locations in the wake as in the previous three figures. As in the case of the velocity profiles, the data obtained on the baseline and fine grids show minor differences. Experimental data was only available for the streamwise component. As with the velocity profiles, the agreement between computation and experiment is good at $x/D = 2.5$ and deteriorates gradually further downstream. In particular, at $x/D = 6.5$, the experimental streamwise profile only exhibits a very slight peak at about $y/D = 1.0$, whereas the computed profiles show a peak at about $y/D = 0.5$. It is interesting to note that classical far-wake-cylinder experimental data for the streamwise Reynolds stress do show a distinct peak at $\xi_2 = y/(xD)^{1/2}$ of about 0.15. The computed peak at $x/D = 6.5$ occurs at about $\xi_2 = 0.20$. Here, the fictitious starting length of the wake upstream of the cylinder has been omitted (this would slightly decrease the value of ξ_2 at which the computed peak occurs but would have little effect on the location of the experimental peak in the far wake). Additionally, the computed peak-to-centerline ratio (streamwise Reynolds stress) is 1.33, and the far-wake data yield a ratio of about 1.3.

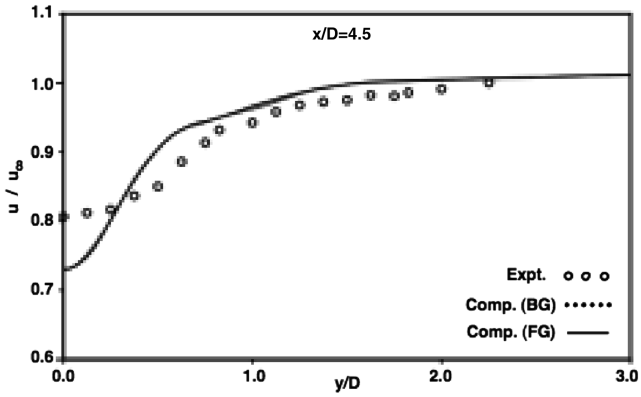

Fig. 22 Profile of mean streamwise velocity at $x/D = 4.5$.

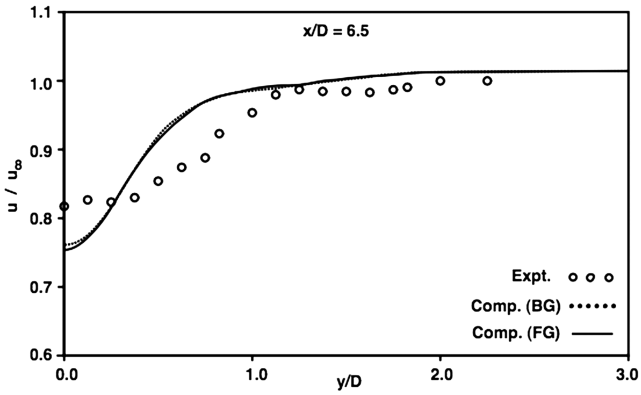

Fig. 23 Profile of mean streamwise velocity at $x/D = 6.5$.

Extracting the Coherent Component of Wake Fluctuations via Filtering

The near wake is of practical interest from the point of view of trailing-edge design, and the intermediate wake is of interest in turbomachinery in understanding and predicting flow transition and unsteady loads on downstream airfoils. The magnitude of the coherent fluctuation and its contribution to the total fluctuations in the velocity and pressure are of particular interest in determining the unsteady loads to be used in design.

The phase-averaging method used here to extract the coherent component is similar to that of Matsumura and Antonia ([5]). Phase at any point along the centerline is determined using the time variation of the cross-stream component of velocity v. First, the v-signal was filtered using a low-pass filter with the cutoff frequency set at 5.25 times the shedding frequency. This rather large cutoff frequency was chosen because the corresponding energy spectrum showed distinct peaks at three and five times the shedding frequency (although these peaks were substantially lower than the one at shedding frequency). The time instants at which the filtered signal v_f crosses zero, t_i, were then determined. The phase θ is then computed exactly as in [5]:

$$\theta = \pi(t - t_{i-1})/(t_i - t_{i-1}) \qquad t_{i-1} \le t \le t_i, \qquad v_f \ge 0.0$$

$$\theta = \pi + \pi(t - t_i)/(t_{i+1} - t_i) \qquad t_i \le t \le t_{i+1}, \qquad v_f \le 0.0$$

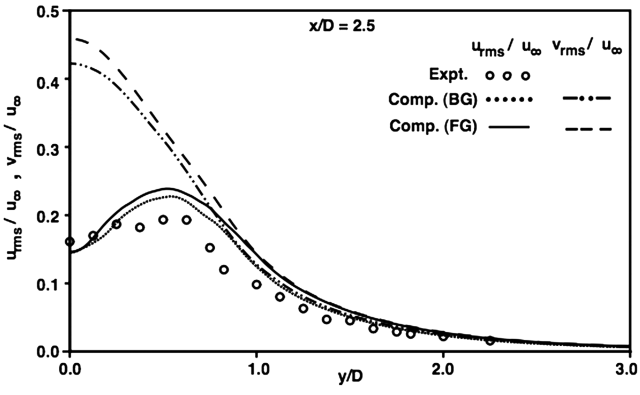

Fig. 24 Profiles of streamwise and cross-stream Reynolds stresses at $x/D = 2.5$.

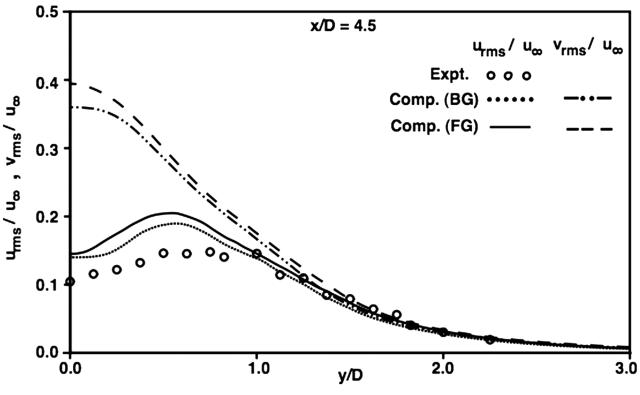

Fig. 25 Profiles of streamwise and cross-stream Reynolds stresses at $x/D = 4.5$.

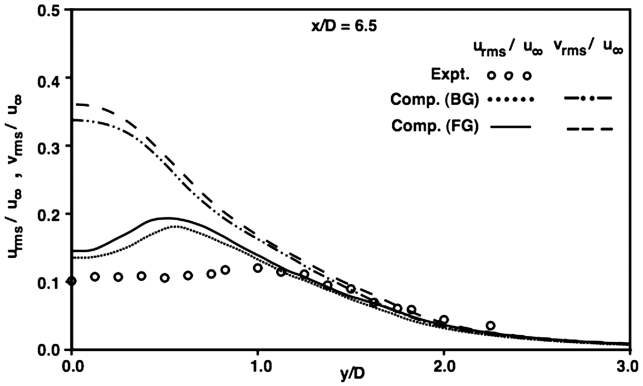

Fig. 26 Profiles of streamwise and cross-stream Reynolds stresses at $x/D = 6.5$.

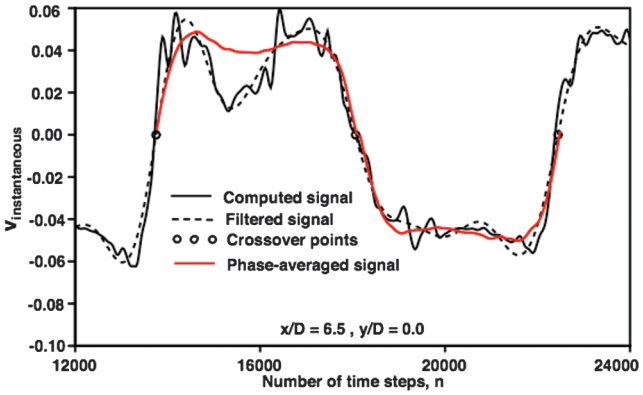

Fig. 27 The computed, filtered, and phase-averaged waveforms of the cross-stream velocity v, and the crossover points of the filtered signal at $x/D = 6.5, y/D = 0.0$.

The time intervals between the crossing points were then dilated or compressed as necessary so that they were all equal to half the shedding period. The original data between were then interpolated onto an equispaced partitioning in time and phase averaged. The data were also averaged in the spanwise direction. Figure 27 shows the original data at the point $x/D = 6.5$, $y/D = 0.0$, obtained over 12,000 consecutive time-steps for this example. The filtered signal and its crossing points and the phase-averaged signal are also included in this figure. Figure 28 shows the original signal and the turbulent component that is obtained by subtracting the filtered signal from the original signal.

The ratio of the energies in the coherent and total signals (v component) was found to be 93.7, 95.0, and 92.3% at the locations $x/D = 2.5$, 4.5, and 6.5, respectively. Some variations in the percentages can be expected with increasing sample sizes. It should

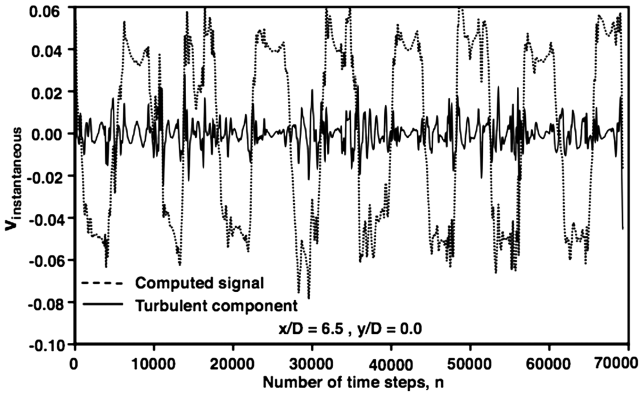

Fig. 28 The computed waveform and the turbulent component of the cross-stream velocity over eight shedding periods at $x/D = 6.5$, $y/D = 0.0$.

be noted that even though only 7.7% of the energy at $x/D = 6.5$ is contained in the turbulent component, because the energy is proportional to the square of the amplitude, the approximate average amplitude of turbulent fluctuation should be about a quarter of the amplitude of the coherent component. This is evident in Fig. 28. Although a slight increase in the ratio is observed between $x/D = 2.5$ and 4.5 before a more significant reduction is obtained between $x/D = 4.5$ and 6.5, the actual energy contained in the coherent component (normalized by the square of the free-stream velocity) takes on the values 0.197, 0.148, and 0.120 at the locations $x/D = 2.5$, 4.5 & 6.5, respectively (a monotonic decrease). Thus, a 40% reduction in the energy associated with the coherent component is obtained between the streamwise locations $x/D = 2.5$ and 6.5.

The computed ratio of the energies in the coherent and total signals for the case of the cylinder at $Re_D = 5830$, along the centerline, at the locations $x/D = 10.0$, 20.0, and 40.0 are 80.6, 65.0, and 47.8%, respectively. The corresponding experimental values from [5] are 85.3, 70.7, and 49.0%. The two sets of data demonstrate the ability of the methodology used here to compute this ratio accurately.

Conclusions

The near wake of a flat plate with a circular trailing edge is investigated via DNS at a Reynolds number of 32,000. The boundary layers on the upper and lower surfaces toward the end of the plate are turbulent. There are several earlier experimental investigations in which thin plates with turbulent boundary layers are used to create the wake. This results in large θ/D values. Here, the emphasis is on relatively thick plates with blunt trailing edges, which result in θ/D values less than unity. Such flows are of considerable engineering interest, particularly in turbomachinery. The characteristics of the very near wake are of importance in trailing-edge design, and the near/intermediate wake is of interest in computing flow transition and the unsteady loads on downstream airfoils. The computations are performed with a high-order accurate upwind-biased finite-difference scheme that has been successfully used in the past for DNS of cylinder wakes and transitional/turbulent flow on flat plates and turbine airfoils.

Results in the form of contour plots of instantaneous and time-averaged velocities and vorticity, contours of Reynolds stresses in the wake, turbulence statistics on the plate and in the wake, and the ratio of energies in the coherent and total velocity signals in the wake are provided. Results obtained from earlier direct numerical simulations for a flat plate at the lower Reynolds number of $Re_D = 3900$ are compared with computed cylinder wake flow at the same Reynolds number and thin-plate wakes. The turbulent boundary layers on the plate were found to reduce the size of the wake recirculation region, move the point of separation of the boundary layer downstream, and reduce both streamwise and cross-stream Reynolds stresses along the centerline by a factor of two to four compared with the cylinder. Along the wake centerline, the thin-plate wake shows the cross-stream component of Reynolds stress to be smaller than the streamwise component. Both the cylinder and the thick plate exhibit the opposite trend, with the streamwise component being much smaller than the cross-stream component. This is mainly because Karman shedding is essentially nonexistent in the thin-plate wake. The comparisons made here with the thin-plate results and those of the cylinder demonstrate that the thick plate while possessing aspects of both the aforementioned flows has its own unique features.

The computation of primary interest here was performed at the much larger Reynolds number of $Re_D = 32,000$. An important objective was to compare the computed wake-turbulence statistics with existing experimental data. This computation was performed on both a baseline grid and a fine grid as part of a grid-refinement exercise. The Reynolds number based on the boundary-layer momentum thickness and the shape factor near the end of the plate are close to that obtained in the experiment. The computed mean velocity profiles at this location on the plate agree well with the log law and fairly well with the experimental data. The computed streamwise Reynolds-stress profiles at this location also agree well with the experimental data, thus establishing the similarity of the

computed and experimental boundary layers just before they detach from the plate surface. The computed velocity and Reynolds-stress profiles in the wake agree well with experimental data in the very near wake but differ somewhat further downstream. The computed wake-velocity statistics obtained on the baseline and refined grids are only slightly different. Additional refinement of the wake grid is not expected to yield velocity statistics that are closer to the experimental data. The remaining quantitative differences are most probably because of differences in the computational and experimental configurations that are discussed in the paper.

The near wake was also explored using contour plots of instantaneous and time-averaged spanwise vorticity and velocity and contour plots of the Reynolds-stress components. Collectively, they show a rapid growth of the wake region caused by Karman shedding, embedding of the turbulent structures within the larger Karman vortices, considerable vortical activity near the base of the circular trailing edge, the breakdown of the detached shear layers, the location of the mean boundary-layer detachment point at about 15 degrees past the vertical, a relatively small recirculation region and minimal acceleration on the free-stream side of the shear layers compared with the cylinder wake at $Re_D = 3900$, and high Reynolds-stress values within the shear layers with maxima/minima occurring away from the wake centerline for the streamwise and shear-stress components.

Acknowledgments

The author thanks C. R. Smith and A. Haji-Haidari for the experimental data used in this study.

References

[1] Marcu, B., Hadid, A., Lin, P., Balcazar, D., Rai, M. M., and Dorney, D. J., "Toward Rocket Engine Components with Increased Strength and Robust Operating Characteristics," *41st AIAA/ASME/SAE/ASEE Joint Propulsion Conference and Exhibit*, Paper 2005-4449, Tucson, AZ, 10–13 July 2005.

[2] Cantwell, B., and Coles, D., "An Experimental Study of Entrainment and Transport in the Turbulent Near Wake of a Circular Cylinder," *Journal of Fluid Mechanics*, Vol. 136, 1983, pp. 321–374. doi:10.1017/S0022112083002189

[3] Wei, T., and Smith, C. R., "Secondary Vortices in the Wake of Circular Cylinders," *Journal of Fluid Mechanics*, Vol. 169, 1986, pp. 513–533. doi:10.1017/S0022112086000733

[4] Unal, M. F., and Rockwell, D., "On Vortex Formation from a Cylinder. Part 1. The Initial Instability," *Journal of Fluid Mechanics*, Vol. 190, 1988, pp. 491–512. doi:10.1017/S0022112088001429

[5] Matsumura, M., and Antonia, R. A., "Momentum and Heat Transport in the Turbulent Intermediate Wake of a Circular Cylinder," *Journal of Fluid Mechanics*, Vol. 250, 1993, pp. 651–668. doi:10.1017/S0022112093001600

[6] Lorenco, L. M., and Shih, C., "Characteristics of the Plane Turbulent Near Wake of a Circular Cylinder. A Particle Image Velocimetry Study," private communication.

[7] Ong, L., Wallace, J., and Moin, P., "The Velocity and Vorticity Fields of the Turbulent Near Wake of a Circular Cylinder," NASA TM-110513, 1995.

[8] Beaudan, P., and Moin, P., "Numerical Experiments on the Flow past a Circular Cylinder at Sub-Critical Reynolds Number," Department of Mechanical Engineering, Stanford Univ., Rept. TF-62, Palo Alto, CA, 1994.

[9] Lin, J.-C., Towfighi, J., and Rockwell, D., "Instantaneous Structure of the Near-Wake of a Circular Cylinder: On the Effect of Reynolds Number," *Journal of Fluids and Structures*, Vol. 9, 1995, pp. 409–418. doi:10.1006/jfls.1995.1023

[10] Lin, J.-C., Vorobieff, P., and Rockwell, D., "Three-Dimensional Patterns of Streamwise Vorticity in the Turbulent Near-Wake of a Cylinder," *Journal of Fluids and Structures*, Vol. 9, 1995, pp. 231–234. doi:10.1006/jfls.1995.1012

[11] Mittal, R., and Moin, P., "Suitability of Upwind-Biased Finite-Difference Schemes for Large-Eddy Simulation of Turbulent Flows," *AIAA Journal*, Vol. 35, No. 8, 1997, pp. 1415–1417. doi:10.2514/2.253

[12] Kravchenko, A. G., and Moin, P., "Numerical Studies of Flow Over a Circular Cylinder at $Re_D = 3900$," *Physics of Fluids*, Vol. 12, No. 2, 2000, pp. 403–417. doi:10.1063/1.870318

[13] Ma, X., Karamanos, G. -S., and Karniadakis, G. E., "Dynamics and Low-Dimensionality of a Turbulent Near Wake," *Journal of Fluid Mechanics*, Vol. 410, 2000, pp. 29–65. doi:10.1017/S0022112099007934

[14] Prasad, A., and Williamson, C. H. K., "The Instability of the Shear Layer Separating from a Bluff Body," *Journal of Fluid Mechanics*, Vol. 333, 1997, pp. 375–402. doi:10.1017/S0022112096004326

[15] Dong, S., Karniadakis, G. E., Ekmekci, A., and Rockwell, D., "A Combined Direct Numerical Simulation-Particle Image Velocimetry Study of the Turbulent Near Wake," *Journal of Fluid Mechanics*, Vol. 569, 2006, pp. 185–207. doi:10.1017/S0022112006002606

[16] Wissink, J. G., and Rodi, W., "Numerical Study of the Near Wake of a Circular Cylinder," *International Journal of Heat and Fluid Flow*, Vol. 29, 2008, pp. 1060–1070. doi:10.1016/j.ijheatfluidflow.2008.04.001

[17] Williamson, C. H. K., "Vortex Dynamics in the Cylinder Wake," *Annual Review of Fluid Mechanics*, Vol. 28, 1996, pp. 477–539. doi:10.1146/annurev.fl.28.010196.002401

[18] Rai, M. M., "Toward Direct Numerical Simulations of Turbulent Wakes," *46th AIAA Aerospace Sciences Meeting*, AIAA Paper 2008-0544, Reno, NV, Jan. 7–10 2008.

[19] Rai, M. M., "A Computational Investigation of the Instability of the Detached Shear Layers in the Wake of a Circular Cylinder," *38th AIAA Fluid Dynamics Conference*, AIAA Paper 2008-4391, Seattle, WA, 23–26 June 2008.

[20] Chevray, R., and Kovasznay, L. S. G., "Turbulence Measurements in the Wake of a Thin Flat Plate," *AIAA Journal*, Vol. 7, 1969, pp. 1641–1643. doi:10.2514/3.5461

[21] Madavan, N. K., and Rai, M. M., "Direct Numerical Simulation of the Turbulent Wake of an Infinitely Thin Flat Plate," *45th AIAA/ASME/SAE/ASEE Joint Propulsion Conference*, AIAA Paper 2009-4929, Denver, CO, 2–5 Aug. 2009.

[22] Andreopoulos, J., and Bradshaw, P., "Measurement of Interacting Turbulent Shear Layers in the Near Wake of a Flat Plate," *Journal of Fluid Mechanics*, Vol. 100, 1980, pp. 639–668. doi:10.1017/S0022112080001322

[23] Bradshaw, P., "Prediction of the Turbulent Near Wake of a Symmetrical Aerofoil," *AIAA Journal*, Vol. 8, 1970, pp. 1507–1508. doi:10.2514/3.5931

[24] Alber, I. E., "Turbulent Wake of a Thin Flat Plate," *AIAA Journal*, Vol. 18, No. 9, 1980, pp. 1044–1051. doi:10.2514/3.50853

[25] Ramaprian, B. R., Patel, V. C., and Sastry, M. S., "The Symmetric Turbulent Wake of a Flat Plate," *AIAA Journal*, Vol. 20, No. 9, 1982, pp. 1228–1235. doi:10.2514/3.7972

[26] Haji-Haidari, A., and Smith, C. R., "Development of the Turbulent Near Wake of a Tapered Thick Flat Plate," *Journal of Fluid Mechanics*, Vol. 189, 1988, pp. 135–163. doi:10.1017/S0022112088000941

[27] Haji-Haidari, A., and Smith, C. R., "A Comparative Study of the Development of the Turbulent Near Wake Behind a Thick Flat Plate with both a Circular and Tapered Trailing Edge Geometry," Department of Mechanical Engineering and Mechanics, Lehigh University, Rept. FM-6, Bethlehem, PA, 1984.

[28] Rai, M. M., "Direct Numerical Simulation of Transitional and Turbulent Flow on a Turbine Airfoil," *42nd AIAA/ASME/SAE/ASEE Joint Propulsion Conference*, AIAA Paper 2006-4460, Sacramento, CA, 9–12 July 2006 (to be published in *AIAA Journal of Propulsion and Power*).

[29] Rai, M. M., and Moin, P., "Direct Numerical Simulation of Transition and Turbulence in a Spatially Evolving Boundary Layer," *Journal of Computational Physics*, Vol. 109, No. 2, 1993, pp. 169–192. doi:10.1006/jcph.1993.1210

[30] Rai, M. M., "Toward Direct Numerical Simulations of Airfoil Wakes," *44th AIAA/ASME/SAE/ASEE Joint Propulsion Conference*, AIAA Paper 2008-5215, Hartford, CT, 21–23 July 2008.

J. Oefelein
Associate Editor